Volume 6
Number 10
21 May 2025
Pages 3005–3356

Materials Advances

rsc.li/materials-advances

ISSN 2633-5409

ROYAL SOCIETY OF CHEMISTRY

PAPER

Sherine O. Obare, Dennis LaJeunesse *et al.*
Enhanced thermal and structural properties of bacterial cellulose with $MgAl_2O_4$ nanoparticles integration

Materials Advances

ROYAL SOCIETY OF CHEMISTRY

PAPER

View Article Online
View Journal | View Issue

Check for updates

Cite this: *Mater. Adv.*, 2025, 6, 3063

Enhanced thermal and structural properties of bacterial cellulose with $MgAl_2O_4$ nanoparticles integration†

Abed Alqader Ibrahim,[a] Anthony L. Dellinger,[abc] Jacob Coscarelly,[a] Gayani Pathiraja,[a] Sherine O. Obare*[a] and Dennis LaJeunesse*[a]

Received 15th November 2024,
Accepted 19th March 2025

DOI: 10.1039/d4ma01130a

rsc.li/materials-advances

Bacterial cellulose (BC), a biogenic nanomaterial with a three-dimensional reticulated architecture, serves as a dynamic platform for next-generation composites. This study presents an advanced BC-based hybrid material integrated with magnesium-doped aluminum oxide ($MgAl_2O_4$) nanoparticles, synthesized through a co-precipitation method. Rigorous characterization *via* TEM-EDS, SEM, XPS, DSC, and XRD elucidates the morphological, elemental, and structural properties of the nanoparticles. Thermal behavior and phase transitions were explored using DSC for both the NPs and the BC-based hybrid material (BC–$MgAl_2O_4$). In-depth surface and structural analyses of the BC–$MgAl_2O_4$ composite was performed using contact angle measurements, XRD, and SEM-EDS. The results demonstrate that the integration of $MgAl_2O_4$ enhances material strength, thermal resistance, and hydrophobicity, driven by synergistic nano-bio interactions. These findings establish a foundation for customized multifunctional composite materials with potential applications in biomedical scaffolding, environmental remediation, and nanosensing.

Open Access Article. Published on 28 March 2025. Downloaded on 5/19/2026 12:03:56 AM.
This article is licensed under a Creative Commons Attribution 3.0 Unported Licence.

The research of nanocomposites has emerged as a critical focus in modern material science, bridging the gap between nanoscale innovations and practical applications. Among these bacterial cellulose (BC) produced by specific bacterial species, such as *Gluconacetobacter hansenii*, through a fermentation process, has garnered attention due to the high purity, crystallinity, mechanical strength, and biocompatibility of this biopolymer.[1] BC distinguishes itself from plant-derived cellulose by its unique nanostructured fiber network, which imparts superior mechanical properties and pronounced hydrophilicity, making it a versatile candidate for diverse applications across biomedicine, electronics, and environmental engineering.[2–4]

While BC has been extensively investigated for its mechanical strength, biocompatibility, and crystalline structure, recent research has concentrated on incorporating nanoparticles (NPs) to augment and diversify these properties.[5] This approach leverages the high surface area and reactive nature of NPs to introduce novel functionalities to BC or enhance the intrinsic properties of the NPs. Previous studies have shown the synergistic effects of incorporating NPs into BC, revealing significant improvements in material properties.[6] The inclusion of metallic NPs, such as silver (Ag) and zinc oxide (ZnO), in BC have been extensively studied for their antibacterial properties. For instance, Baker *et al.* demonstrated that the bio-functionalization of Ag and ZnO nano-bactericides onto cellulose films resulted in effective bactericidal activity against multiple drug-resistant pathogens, highlighting the potential of metal NPs to enhance the physicochemical properties of BC.[7] Similarly, Shaaban *et al.* reported that BC impregnated with green-synthesized silver NPs exhibited significant antibacterial activity against *Staphylococcus aureus* and *Pseudomonas aeruginosa*, reinforcing the effectiveness of BC-AgNPs hybrids in combating bacterial infections.[8] Our prior research has reported and characterized CuO nanoleaves modified BC, demonstrating the formation of a mechanically stable nanofiber matrix.[9] Moreover, Melnikova *et al.* developed a nanocomposite of BC with zinc oxide (ZnO) NPs and betulin diphosphate (BDP) to assess the biological activity of the composite in a thermal burn rat model.[10] Their findings demonstrated that such BC-based hybrid material hold significant potential for medical applications. Additional research has shown that the addition of functional NPs like titanium dioxide (TiO_2) or silicone dioxide (SiO_2) can enhance the mechanical strength, thermal stability, and photocatalytic activity of BC.[11,12]

Magnesium (Mg) based alloys have been explored for several biomedical applications due to their structural stability, biocompatibility as well as their biodegradability. Researchers have made efforts to use Mg in the biomedical field as a biodegradable

[a] *Department of Nanoscience, Joint School of Nanoscience and Nanoengineering, University of North Carolina at Greensboro, Greensboro, NC, 27401, USA. E-mail: soobare@uncg.edu, drlajeun@uncg.edu*
[b] *Kepley Biosystems Incorporated, Greensboro, NC, 27214, USA*
[c] *AT Research Partners, Burlington, NC, 27217, USA*

† Electronic supplementary information (ESI) available. See DOI: https://doi.org/10.1039/d4ma01130a

© 2025 The Author(s). Published by the Royal Society of Chemistry

Open Access Article. Published on 28 March 2025. Downloaded on 5/19/2026 12:03:56 AM.
This article is licensed under a Creative Commons Attribution 3.0 Unported Licence.

material that is required in clinics.[13] A recent study by Topuza *et al.* has used $Ti_3C_2T_x$ (MXene) functionalized hydroxyapatite (HA) and halloysite nanotube (HNT)-reinforced poly(lactic acid) (PLA) coatings on magnesium substrates to improve corrosion resistance and antibacterial activity.[14]

Moreover, some metal oxides, also known as ceramics, have shown a unique behavior at high temperatures. A well-known member of this family, Magnesium aluminate ($MgAl_2O_4$), exhibited very promising properties such as a high working temperature that reaches up to 2000 °C, high strength, as well as low thermal conductivity.[15] While most BC-based hybrid material have been designed for applications requiring antibacterial or optical enhancements, this study diverges from these approaches by emphasizing the structural robustness and thermal behavior imparted by the inclusion of $MgAl_2O_4$.[16] These findings provide new insights into the potential of Mg-doped composites for biomedical scaffolds and high-temperature applications. Moreover, the integration of NP into BC represents a novel research direction for developing advanced materials with tailored properties that are adaptable for diverse industrial and technological applications, including filtration, packaging, and sensor technology. Unlike previously studied NPs, $MgAl_2O_4$ offers distinct advantages, such as enhanced thermal stability, crystallinity, and mechanical strength, positioning it as a promising candidate for applications requiring durable and thermally stable materials. This study is the first to investigate the enhancement of thermal stability, crystallinity, and surface hydrophobicity of BC through the incorporation of $MgAl_2O_4$ NPs, highlighting its potential for advanced composite material development.

Experimental section

Materials

Aluminum nitrate nonahydrate ($Al(NO_3)_3$) (Sigma Aldrich, ACS reagent, ≥98%), magnesium chloride hexahydrate ($MgCl_2$) (Sigma, minimum 99.0%), sodium hydroxide (NaOH) (Supelco, EMPLURA pellets), 2% (w/v) glucose (Thermo Scientific, anhydrous, 99%), 0.5% (w/v) yeast extract (Fisher Bioreagents), 0.5% (w/v) peptone (Fisher Bioreagents, granulated), 0.27% (w/v) sodium phosphate dibasic (Fisher Bioreagents, white granules), and 0.115% (w/v) citric acid monohydrate (Fisher Scientific, powder).

Synthesis of $MgAl_2O_4$ NPs

The co-precipitation technique was used to synthesize $MgAl_2O_4$ NPs. Briefly, 0.2 M solutions of $Al(NO_3)_3$ and $MgCl_2$ were individually dissolved in 5 mL of deionized water (diH_2O) and mixed with continuous stirring at 80 °C until completely dissolved. A 0.2 M NaOH solution was then added dropwise, under vigorous stirring, to adjust the pH to 12 and obtain complete precipitation. The reaction mixture was stirred for 3 hours, allowing sufficient time for the co-precipitation of the metal hydroxides. After cooling to room temperature, the white precipitate formed was centrifuged and washed three times with deionized water, followed by ethanol, to remove any unreacted species or impurities. The washing steps were essential to ensure the purity of the final product. The resulting

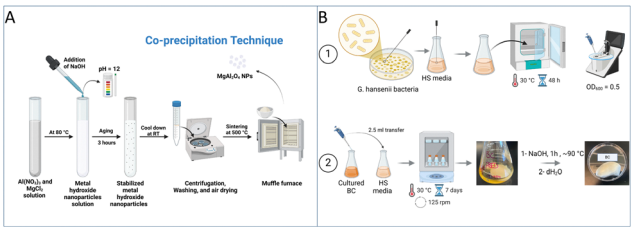

Fig. 1 Schematic representation of (A) $MgAl_2O_4$ NP synthesis and (B) BC synthesis.

product was dried in air for 24 hours and then annealed at 500 °C for 3 hours to obtain $MgAl_2O_4$ NPs (Fig. 1A). Several challenges were encountered during the synthesis of $MgAl_2O_4$ NPs, particularly related to NP agglomeration during the drying and annealing processes which could also be attributed to the charge of these NPs (See ESI†). The use of ethanol in the washing steps helped mitigate this issue by reducing surface tension between the particles. Additionally, temperature control during annealing was crucial, as overheating led to sintering, which decreased the surface area of the NPs.[17] To ensure consistency, multiple batches of NPs were synthesized under identical conditions, and their properties were cross-checked using TEM and XRD to confirm reproducibility.The actual yield of the $MgAl_2O_4$ NPs was calculated to be 85.3% indicating efficient synthesis process.

Bacterial cellulose preparation

Gluconacetobacter hansenii bacteria was cultured in Hestrin–Schramm (HS) medium containing 2% (w/v) glucose, 0.5% (w/v) yeast extract, 0.5% (w/v) peptone, 0.27% (w/v) sodium phosphate dibasic, and 0.115% (w/v) citric acid. An initial culture was inoculated in 25 mL of HS medium and incubated at 30 °C for 2 days, reaching an OD_{600} of 0.5. Subsequently, 2.5 mL of this culture was transferred into a 125 mL Erlenmeyer flask containing 22.5 mL of fresh HS medium and incubated at 30 °C in a shaking incubator set to 125 rpm for 7 days. The resulting BC pellicles were processed in 0.1 M NaOH at ~95 °C for 1 hour to remove bacteria cells and biofilm materials. The pellicles were then rinsed with diH_2O until a neutral pH was achieved and stored at room temperature (Fig. 1B). To create the BC/NP composite materials, the prepared $MgAl_2O_4$ NPs were sonicated in media for 1 hour to break up any NP aggregates before being added to the HS medium at concentrations of 5 mg, 10 mg, and 20 mg. Sonication was employed to improve the dispersion of the NPs within the BC matrix, preventing uneven distribution and agglomeration during the composite formation. After integration, the BC pellicles were allowed to grow in the NP-enriched medium for an additional 7 days. This process ensures that the BC pellicles formed around the nanoparticles, creating homogeneous BC–$MgAl_2O_4$ NPs hybrids. In contrast to other BC preparation methods, this technique avoids complications caused by factors such as the pore size of the BC, the size of the NPs, and diffusion rate of the particles into a preformed BC pellicles. This is because our method involves the cellulose pellicles to be formed around the majority of the material suspended in the culture media.

© 2025 The Author(s). Published by the Royal Society of Chemistry

Open Access Article. Published on 28 March 2025. Downloaded on 5/19/2026 12:03:56 AM.
This article is licensed under a Creative Commons Attribution 3.0 Unported Licence.

Material characterization

The morphology and crystallinity, including lattice parameters, local framework structure, and selective area diffraction patterns of the NPs and composite materials were analyzed using transmission electron microscopy (TEM) with an accelerating voltage of 200 kV from JEOL 2100PLUS with STEM/EDS capabilities. This technique enabled a detailed examination of both the morphology and chemical composition of as-synthesized $MgAl_2O_4$ NPs. For XPS measurements, the NP samples were dried in air on a silicon (Si) wafer sample holder. Elemental compositions were determined using XPS with an Escalab Xi^+ (Thermo Scientific). The samples were also drop-casted on a Si wafer to obtain the micro-elemental compositions and were matched with the XPS elemental survey analysis. SEM/EDS analysis was performed to analyze all NPs and BC morphologies using a JEOL JSM-IT800 FESEM with Oxford Ulti Max EDS (Energy Dispersive X-ray Spectroscopy).The samples were drop-casted on a Si wafer and then sputter-coated with a 7 nm gold/palladium layer to prevent charging in the microscope. X-ray data was acquired at 10 kV in low vacuum mode with a chamber pressure of 50 Pa. Dynamic light scattering (DLS) and zeta potential measurements were performed to assess the hydrodynamic diameter and surface charge of the $MgAl_2O_4$ NPs. DLS was conducted using a Malvern Zetasizer ZEN3600 with measurements taken in deionized water at 25 °C in triplicates. Zeta potential was measured to determine particle stability and dispersion behavior in aqueous solutions. Powder X-ray diffraction (XRD) data was collected on a Rigaku Gemini a single crystal diffractometer to further analyze the crystalline structures. A TA Q200 digital scanning calorimeter (DSC) was used to study the thermal properties of the materials. Contact angles for the BC-NP composites were performed using a Rame Hart Model 260 Goniometer. A TA Instruments TGA 5500 was also used to further study and confirm the thermal properties of the materials in the temperature range of 25–800 °C heating at the rate of 25° per minute. Ten contact angle measurements were taken within one second per drop, then averaged, and three drops were placed on each membrane to calculate an overall average contact angle, with the highest average of each of the three drops.

Results and discussion

TEM analysis

The morphology, structural details, and chemical composition of synthesized $MgAl_2O_4$ NPs were investigated using TEM/STEM techniques. The TEM image (Fig. 2A) shows a representitive $MgAl_2O_4$ cluster, indicating the characteristic structure of $MgAl_2O_4$ NPs. The angular-dark field scanning transmission electron microscopy (ADF-STEM) image (Fig. 2B) provides additional evidence of the porosity within these NPs. The STEM combined with EDS analysis reveals the distribution of each metal oxide in $MgAl_2O_4$ NP clusters, showing distinct elemental mapping. The corresponding elemental maps (Fig. 2C–F) demonstrate the spatial distribution of Al and Mg within the NPs. The analysis suggests a higher concentration of Al compared to Mg, consistent with the chemical composition of the $MgAl_2O_4$ NPs.

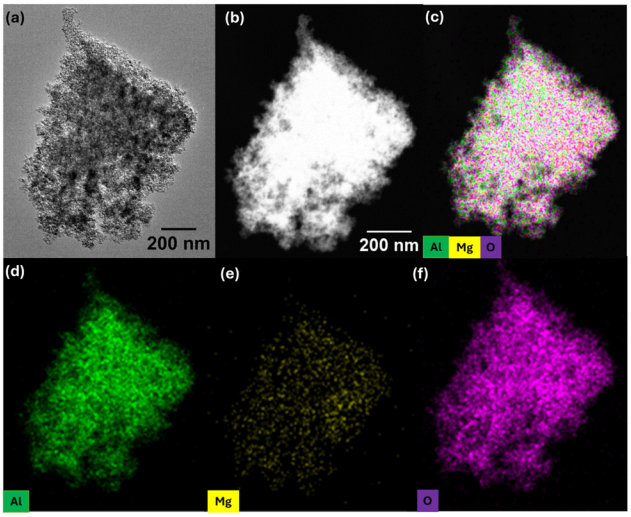

Fig. 2 (a) Transmission electron microscopy (TEM) image of $MgAl_2O_4$ NPs showing a cluster, accompanied by (b) angular-dark field scanning transmission electron microscopy (ADF-STEM) imaging, illustrating porosity within the NPs. Corresponding energy-dispersive X-ray spectroscopy (EDS) elemental mapping (c)–(f) confirms the spatial distribution of Al, Mg, and O within the NP clusters.

X-ray photoelectron spectroscopy

The surface chemistry and oxidation states of as-synthesized $MgAl_2O_4$ NPs were determined *via* XPS analyses. The XPS survey spectra, illustrated in Fig. 3A, confirmed the presence of the primary elements, including Al, Mg, and O. In the Al 2p region (Fig. 3B), a characteristic peak of Al^{3+} ions was observed at 74.5 eV corresponding to aluminum oxide (Al_2O_3), which aligns with known data from Al_2O_3.[18,19] Additional deconvoluted peak at higher binding energies indicate the presence of surface hydroxyl group (Al–OH) or aluminium hydroxide $Al(OH)_3$ which suggests partial surface oxidation or surface defects.[20] The Mg 1s spectrum (Fig. 3C) exhibited a

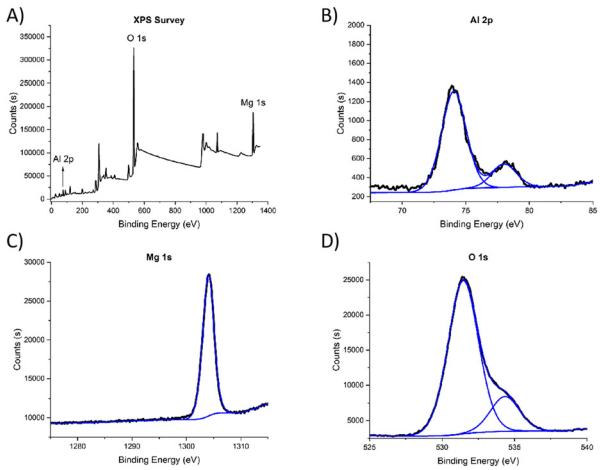

Fig. 3 X-ray photoelectron spectroscopy (XPS) (A) survey spectrum of $MgAl_2O_4$ NPs confirms the presence of Al, Mg, and O. High-resolution spectra show (B) Al^{3+} ion peaks in the Al 2p region, (C) a single peak corresponding to Mg^{2+} in the Mg 1s spectrum, and (D) O^{2-} and peroxide doublet peaks in O 1s spectrum.

Open Access Article. Published on 28 March 2025. Downloaded on 5/19/2026 12:03:56 AM. This article is licensed under a Creative Commons Attribution 3.0 Unported Licence.

single prominent peak at 1304.3 eV, corresponding to Mg^{2+}, which is consistent with those previously reported values for magnesium oxide (MgO).[21] The O 1s spectrum (Fig. 3D) exhibited two distinct peaks at 531.5 eV and 534.5 eV, attributable to the lattice O^{2-} and surface hydroxyl (–OH) and peroxide (O_2^{2-}) species respectively, as identified in previous studies.[21] Furthermore, the XPS stoichiometric composition (Mg : Al : O) closely match the theoretical ratio of the $MgAl_2O_4$ NPs confirming a successful synthesis of the NPs, as shown in Table S1 (ESI†).

Scanning electron microscopy-energy dispersive X-ray

Scanning electron microscopy (SEM) (Fig. 4(I) and (II)) coupled with energy-dispersive X-ray spectroscopy (EDS) (See ESI†) provided a detailed morphological and compositional analysis of the $MgAl_2O_4$ NPs and BC–$MgAl_2O_4$ composite. The SEM micrographs (Fig. 4(I)) showed a homogeneous distribution of the NPs with a similar size to the TEM results shown in Fig. 2. The uniform and rough surface morphology of the NPs enhances their interaction with the BC matrix, potentially improving adhesion and distribution within the composite. The images revealed significant changes in the morphology of the BC matrix after the incorporation of $MgAl_2O_4$ NPs. In the unmodified BC (Fig. 4(II.A)), the typical nanofibrillar network structure of cellulose was observed, with visible pores between the fibers (as shown in the inset). However, with increasing $MgAl_2O_4$ concentrations (5 mg, 10 mg, and 20 mg), the SEM images (Fig. 4(II.B, C, and D), respectively) showed the presence of densely packed NP clusters embedded within the cellulose matrix. The NPs -modified BC fibers at increasing concentrations are highlighted in the insets of each SEM image.

The incorporation of $MgAl_2O_4$ NPs modified the overall porosity of the BC by filling the inter-fiber gaps, resulting in a more compact structure characterized by the NP clusters. This reduction in pore size is expected to enhance the composite material's structural properties, particularly tensile strength, which is advantageous for structural applications. Additionally, the presence of NPs may improve the barrier properties of the material, further expanding the composite's potential use for filtration or packaging applications.[22–24]

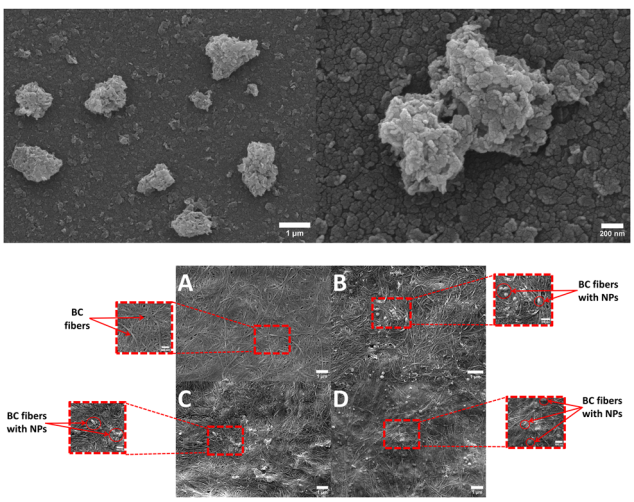

Fig. 4 I: SEM images of $MgAl_2O_4$ NPs at two different magnifications. (Left) The scale bar is 1 µm, and (Right) 200 nm. II: SEM images of (A) Pure BC (B) BC with 5 mg of $MgAl_2O_4$ NPs, (C) BC with 10 mg of $MgAl_2O_4$ NPs, (D) BC with 20 mg of $MgAl_2O_4$ NPs. The scale bar is 1 µm. Insets show the corresponding fibers and NPs-modified fibers images at scale bar of 500 nm.

EDS analysis confirmed the successful incorporation of Mg and Al elements into the BC matrix. The consistent detection of Mg and Al in all modified samples, along with the absence of other significant impurities, supports the homogeneity of the composite material. Notably, the Si peaks observed in some samples are attributed to the Si substrate used during SEM sample preparation and do not indicate contamination of the BC–$MgAl_2O_4$ composite itself.[25]

The increased density of the NP clusters within the BC matrix, especially at higher concentrations, may also affect the composite's optical transparency, making it a potential candidate for applications in flexible electronics or transparent substrates. However, at higher loadings, aggregation of the NPs could hinder uniform dispersion, which may affect the overall performance of the material. Optimizing NP loading and dispersion techniques will be essential for tailoring the composite's properties to meet the requirements for specific applications.[26]

The phenomenon of increased fiber density due to the incorporation of NPs is supported by the findings of Fahma *et al.*, who noted that the presence of NPs within a polymer matrix can lead to enhanced interactions and entanglements among the fibers, resulting in more compact structure.[27] Moreover, the work by Nogi *et al.* emphasizes the importance of fiber packing in achieving high optical transparency in nanofiber papers, which is a direct consequence of reduced light scattering due to densely packed fibers.[28] This principle can be extrapolated to the BC-NP hybrid, where the reduced porosity and increased density may similarly enhance the optical properties of the material, making it suitable for applications in flexible electronics and transparent substrates.[29]

Dynamic light scattering (DLS) and zeta potential analysis

The DLS analysis was performed in triplicate and the results represent the average values. The DLS analysis showed that $MgAl_2O_4$ NPs had an average hydrodynamic diameter of 191.54 ± 1.99 nm with a polydispersity index (PDI) of 0.252 (See ESI†). The low PDI value indicates a relatively uniform particle size distribution, which is essential for achieving stable dispersion within the BC matrix. Moreover, zeta potential measurements indicated a surface charge of +40.86 ± 0.33 mV (See ESI†), suggesting strong electrostatic stability in suspension. The positive zeta potential enhances the dispersion quality and reduces the likelihood of NP aggregation within the BC matrix, which is crucial for maintaining consistent thermal and structural properties across the composite. The high stability indicated by the zeta potential value aligns with the uniform integration observed in SEM images, further supporting the effectiveness of $MgAl_2O_4$ as a stabilizing agent in BC composites.

Differential scanning calorimetry analysis

The DSC analysis provided insights into the thermal stability and phase transitions of the $MgAl_2O_4$ NPs and BC/NP composites

© 2025 The Author(s). Published by the Royal Society of Chemistry

Open Access Article. Published on 28 March 2025. Downloaded on 5/19/2026 12:03:56 AM.
This article is licensed under a Creative Commons Attribution 3.0 Unported Licence.

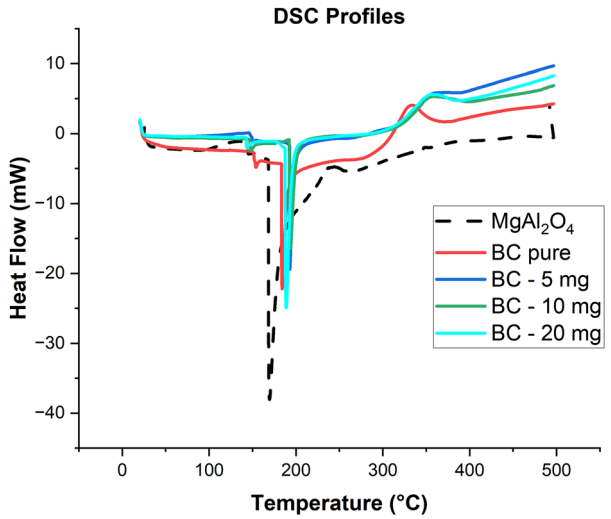

Fig. 5 Differential scanning calorimetry (DSC) profiles ramped from room temperature to 500 °C at 10 °C min^{-1}. Dashed black – NPs; solid red – BC with no NPs; solid magenta – BC with 5 mg of NPs; solid blue – BC with 10 mg of NPs; solid green – BC with 20 mg of NPs.

(Fig. 5). The DSC analysis provided insights into the thermal stability and phase transitions of the $MgAl_2O_4$ NPs and BC/NP composites (Fig. 5). Previous studies have shown a wide variation in the glass transition temperature (T_g) values for semicrystalline materials, particularly BC,[30] even when accounting for the changes in heat capacity due to the percent crystallinity, the initial cooling rate of the material, and the temperature at which the mobile amorphous region and the rigid amorphous region (located at the interface between the crystalline and mobile amorphous regions) transition from a glassy, restricted state to a more mobile state (unfreeze).[31] Moreover, in Silviana *et al.*, the T_g value for NaOH-purified BC was reported as 116 °C,[32] while in George *et al.* it was reported as 41.41 °C.[33] Therefore, the first endothermic peak observed around 156 °C could be attributed to the relaxation of amorphous regions due to the semicrytalline nature of the BC.[34] Notably, a decrease in this temperature was observed with increasing NP loading (5 mg, 10 mg, and 20 mg) suggesting that the incorporation of $MgAl_2O_4$ NPs influences the amorphous nature of the composite, as observed in the SEM images (Fig. 4(II)). The endothermic peak presence in the $MgAl_2O_4$ NPs pattern at 170 °C is attributed to the vaporization of physically absorbed water, as reported in previous DSC results.[35] In a comparable manner, the peaks around 188 °C may also correspond to the release of physically absorbed water in the BC and the BC-NPs hybrids. Furthermore, the exothermic transition for BC starting at 300 °C implies a chemical change occurring which is attributed to the decomposition of the BC due to pyrolysis. Notably, the onset of decomposition was observed at a higher temperature, starting at 320 °C, suggesting enhanced structural and thermal stability in the BC-NPs hybrids. These findings are consistent with previously published decomposition temperature data for BC, further supporting the observed thermal behavior.[36] This crystallinity enhancement may contribute to the higher thermal stability of the BC-NPs hybrid, supporting its suitability for applications in high-temperature environments such as advanced filtration systems or structural composites.[37] The reduced heat capacity of the composites, compared to the individual components, further reinforces the improved stability conferred by the NPs. This phenomenon is consistent with of the higher thermal stability exhibited by the composite materials.[38]

Thermogravimetric analysis (TGA)

The TGA results for the $MgAl_2O_4$ NPs, pure BC, and the BC-NP hybrids with 5 mg, 10 mg, and 20 mg are shown in Fig. 6. The NPs shows high thermal stability indicated by a minimal mass loss through the entire temperature range. The minimal amount of mass loss could be attributed to the moistures impurities from the synthesis process being vaporized as the NPs expand to allow leftover species to escape. The BC and BC-NP hybrids experience a slight mass loss between 50 °C and 250 °C, which can be attributed to the membrane dehydration.[39] Moreover, there is a pseudo-stepwise drop in mass between 300 °C and 350 °C, which is indicative of a chemical reaction.[40] This chemical reaction is the decomposition of the BC into carbon and carbon monoxide through fragmentation of carbonyl and carboxylic bonds from the anhydrous glucose monomers.[41] These results confirm the previous data obtained in the DSC exothermic peaks and match previously reported decomposition temperatures (336 °C) of standard cellulose and BC.[36,42] As $MgAl_2O_4$ NPs loading increases, the onset temperature of the BC degradation decreases, indicating an earlier thermal decomposition. However, the overall mass loss is reduced due to the weight contribution of the NPs, which remain

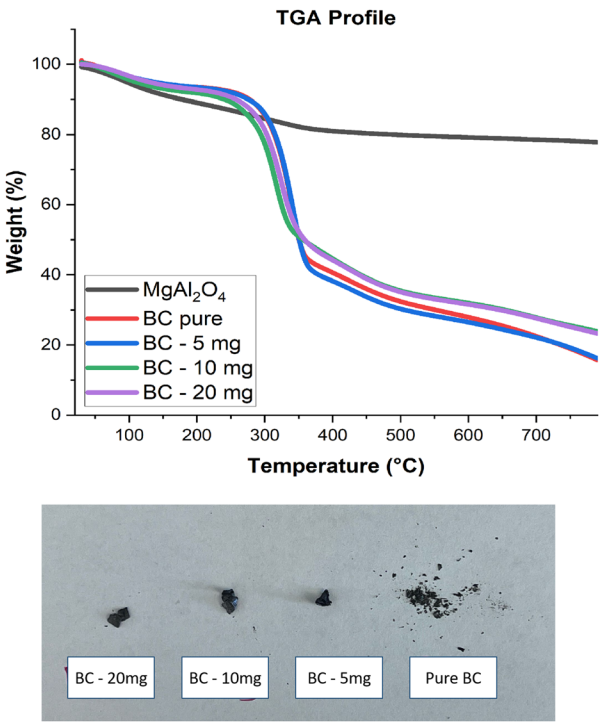

Fig. 6 TGA profile of $MgAl_2O_4$ NPs (black trace), BC (red trace), BC – 5 mg (blue trace), BC – 10 mg (green trace), and BC – 20 mg (purple trace) and representative image of the BC and BC-NPs hybrids after TGA, illustrating the final physical state after thermal degradation.

Open Access Article. Published on 28 March 2025. Downloaded on 5/19/2026 12:03:56 AM.
This article is licensed under a Creative Commons Attribution 3.0 Unported Licence.

thermally stable up to 2000 °C.[43] These findings suggest that the BC-NPs hybrids exhibit enhanced structural stability, as the NPs reinforce the membrane and mitigate its decomposition into volatile by-products, which is also shown in the photographic images in Fig. 6.

The X-ray diffraction (XRD) analysis

The XRD analysis confirmed the formation of the $MgAl_2O_4$ spinel structure (Fig. 7A), where the results present high purity $MgAl_2O_4$ NPs with the diffraction peaks corresponding to the (111), (220), (311), (400), (422), (511), (440), and (620) planes according to reference code (PDF#21-1152).[44]

The sharpness and intensity of these peaks indicate a high degree of crystallinity, which is crucial for maintaining the mechanical stability and uniformity of the NPs.[45,46] This high crystallinity, a result of the optimized annealing process, directly contributes to the enhanced thermal stability observed in the DSC analysis.[47] These well-defined peaks indicate a successful formation of the $MgAl_2O_4$ spinel phase. Such crystallinity is essential for applications requiring stable and uniform NP properties. The crystallite size of the NPs is calculated using the most intense peak (111) according to the Scherrer formula:

$$d = \kappa\lambda/(\beta\cos\theta) \quad (1)$$

where d is the crystallite size of the NPs in nm, κ is the correction factor (0.943), λ is 1.54 Å, β is the full width of the diffraction peak, and θ is the Bragg angle. The calculations shows that the crystallite size is 134.79 nm.[44]

These findings confirmed the effectiveness of the co-precipitation method employed for synthesizing $MgAl_2O_4$ NPs, ensuring their suitability for further modification and application in composite materials. The identification of these peaks aligns with existing literature on $MgAl_2O_4$ spinel structures. For instance, Nguyen *et al.* reported similar findings in their studies on the synthesis of transparent $MgAl_2O_4$ ceramics, where they noted that the XRD patterns exhibited peaks corresponding to the spinel structure, confirming the successful synthesis of single-phase $MgAl_2O_4$.[48] This is significant as the presence of a single-phase spinel structure is essential for optimizing the material's properties for applications in optics and catalysis.[48]

The pure BC (Fig. 7B) displayed two prominent 2θ peaks at 14.5° and 22.8°. These peaks are characteristic of the crystalline regions within the cellulose structure.[49] The peak at 14.5° corresponds to the (110) plane, while the peak at 22.8° is associated with the (200) plane of cellulose.[50–52] These diffraction peaks confirmed the presence of the crystalline phase of BC, reflecting its natural fibrous structure. The observed sharpness and intensity of these peaks indicated a well-ordered arrangement of cellulose chains, which is typical of high-purity BC.

Furthermore, the integration of $MgAl_2O_4$ into BC (Fig. 7B) did not significantly alter the cellulose's characteristic crystallinity, as indicated by the persistence of the BC peaks at 14.5° and 22.8°. This preservation of BC's structure highlights the compatibility of the NPs with the cellulose matrix, ensuring that the unique structural properties of BC are maintained, while introducing additional benefits such as enhanced thermal stability. The well-ordered arrangement of the $MgAl_2O_4$ NPs within the cellulose matrix may also improve the composite's structural integrity, making it a promising candidate for applications in high-performance materials, such as in biomedical scaffolds or filtration systems. The peak at approximately 14.3° is consistent with findings from various studies that have characterized cellulose structures. For instance, in the study of Fang *et al.* similar diffraction peaks at 2θ values of 14.3° and 22.8° for cellulose I (the native form of cellulose) were observed, indicating that the crystalline structure of BC aligns with established cellulose characteristics.[53] Additionally, it was noted that typical peaks for cellulose I are observed around 15° and 22.6°, further supporting the identification of the crystalline phases in BC.[54] These consistent findings across different studies reinforce the reliability of the XRD analysis in confirming the crystalline nature of BC.

The observed XRD patterns, showing only the peaks of BC, can be attributed to the effects of preferred orientation, thin film thickness, substrate influence, NP dispersion, and potential changes in the crystallinity of the embedded NPs. These factors combined can result in the suppression or complete absence of $MgAl_2O_4$ NP peaks in the thin film XRD analysis.[6,55,56] These structural insights from XRD are complemented by the thermal stability findings in the DSC analysis, which further highlight the improved performance of the composite at higher temperatures.

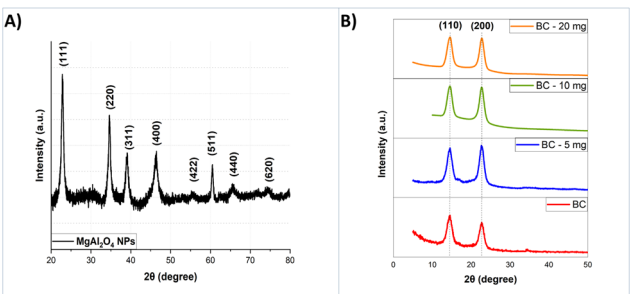

Fig. 7 XRD pattern of (A) Powder $MgAl_2O_4$ NPs and (B) thin-film analysis of BC (red trace), BC – 5 mg (blue trace), BC – 10 mg (green trace), and BC – 20 mg (orange trace).

Contact angle

Contact angle is a principal technique for determining the surface hydrophobicity. When applied to a smooth, flat and inert surfaces, water droplet create an angle that represent the hydrophobicity of the surface.[57] Contact angle measurements (Fig. 8) revealed that the hydrophobicity of the BC membranes increases with the incorporation of $MgAl_2O_4$ NPs. Initially, the contact angle for the pure BC shows an average value of 45.9° ± 0.1. These results match the previously reported pure BC contact angle values reported by Indriyati *et al.* which stated that the pure BC contact angle is 45°.[58] Although the hydrophilic nature of BC might considered an advantage in some applications, it could be a limitation to certain applications such as in the packaging field where a hydrophobic nature is preferred.[58] Incorporating $MgAl_2O_4$ at 5 mg and 10 mg NP, has interestingly increased the contact angle increased up to 75.6° and 76.9°, respectively, suggesting that the surface became

© 2025 The Author(s). Published by the Royal Society of Chemistry

Open Access Article. Published on 28 March 2025. Downloaded on 5/19/2026 12:03:56 AM.
This article is licensed under a Creative Commons Attribution 3.0 Unported Licence.

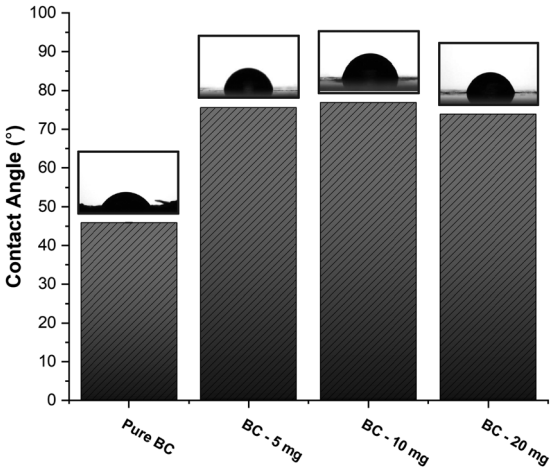

Fig. 8 Mean contact angle of diH_2O on the surface of BC and modified BC membranes. Top left – BC with no NPs; top right – BC with 5 mg of NPs; bottom left – BC with 10 mg of NPs; bottom right – BC with 20 mg of NPs.

more hydrophobic due to the nonpolar nature of the NPs. The reduced interaction between the cellulose and water is consistent with the introduction of metal oxides, which likely decrease the surface energy of the composite. This phenomenon is consistent with findings in the literature, which suggest the incorporation of nonpolar NPs can lead to increased hydrophobicity in polymer matrices.[59]

Interestingly, at a higher NP loading of 20 mg, the contact angle decreased slightly to 73.9°, though it remained higher than that of pure BC. This behaviour suggests a critical point at which further NP incorporation leads to aggregation or uneven dispersion within the cellulose matrix, thus reducing the overall hydrophobic effect. The aggregation at higher concentrations may expose more of the hydrophilic BC surface, counteracting the hydrophobic contribution of the NPs. At higher NP loadings, when the critical point is reached, the negative surface charge of the NPs might lead to repulsive interactions, reducing the overall hydrophobic effect.[60]

This trend highlights the importance of optimizing NP loading to achieve the desired balance between hydrophobicity and material integrity. The enhanced hydrophobicity at optimal NP loadings opens new possibilities for using BC–$MgAl_2O_4$ composites in applications where moisture resistance is critical, such as in packaging materials, membranes, or biosensors.[61]

Conclusions

The incorporation of $MgAl_2O_4$ into BC in this study focuses on thermal stability, crystallinity, and hydrophobicity, offering a distinct advantage over previous studies that emphasized antibacterial or optical properties. For example, Baker *et al.* and Shaaban *et al.* demonstrated significant bactericidal effects with Ag and ZnO NPs.[7,8] However, their work did not explore the thermal or structural stability improvements that are critical for high-temperature and moisture-sensitive applications, which were addressed in this study. The co-precipitation synthesis and integration of $MgAl_2O_4$ NPs altered the morphology, thermal stability, and surface hydrophobicity of the BC, revealing the potential for tailored material properties and advancing the understanding of hybrid materials.

Melnikova *et al.* investigated ZnO NPs in BC for wound healing, showing excellent biological activity but without significant gains in thermal properties.[10] In contrast, the $MgAl_2O_4$ integration in this work enhances both thermal stability and surface hydrophobicity, making it more suitable for filtration and structural applications. Further, several research used TiO_2 to enhance mechanical strength, biomedical applications, and photocatalytic activity, underscoring the versatility of BC composites across various industrial applications.[16,53,62,63] Lastly, Machado *et al.* incorporated resveratrol into BC, resulting in increased biocompatibility for applications in tissue regeneration.[4] Although their work focused on biological applications, this aligns with the potential of our BC–$MgAl_2O_4$ composite to be further explored in biomedical scaffolds, particularly where structural stability and thermal robustness are required. Our findings shows promising properties of the BC-metal oxide hybrid compared with similar studies of BC-based hybrid material, as shown in Table 1.

These findings demonstrate that $MgAl_2O_4$ NPs enhance the BC matrix's structural stability, crystallinity, and surface characteristics, making it suitable for a diverse range of applications. Future directions should focus on scaling production, ensuring long-term stability, and optimizing synthesis and integration processes to facilitate practical deployment and commercial viability. Additionally, exploring the use of other NP types and combinations could yield composites with more diverse properties, tailored for specific applications such as biomedical scaffolds, filtration systems, and electronic sensors.

Table 1 A comparison of this work with relevant studies from the literature

Metal/metal oxide used	Bacterial strain	Thermal stability	Antibacterial activity	Hydrophobicity	Potential applications	Ref.
$MgAl_2O_4$	*Gluconacetobacter hansenii*	Enhanced	Not studied	Increased	Biomedical scaffolds, filtration, high-temp applications	This study
Ag, ZnO	*Komagataeibacter xylinus*	Not studied	Strong effect	Not studied	Antimicrobial coatings, medical applications	7
Ag	*Komagataeibacter xylinus*	Not studied	Strong effect	Not studied	Antimicrobial coatings, medical applications	8
ZnO	*Gluconacetobacter hansenii*	Moderate improvement	Moderate effect	Not studied	Wound healing	64
TiO_2	*Gluconacetobacter xylinus*	Not studied	Strong effect	Not studied	Wound healing	16
TiO_2	*Komagataeibacter hansenii*	Reduced	Not studied	Not studied	Wastewater treatment	63

Open Access Article. Published on 28 March 2025. Downloaded on 5/19/2026 12:03:56 AM. This article is licensed under a Creative Commons Attribution 3.0 Unported Licence.

Author contributions

AAI conceived the study, designed and performed the experiments, interpreted the results, wrote the manuscript, review, and revision. JC performed experiments, interpreted DSC and contact angle, review, and revision. GP performed, analyzed TEM experiments and revision. AD involved in the writing, review, revision of the manuscript and supervision. SO and DL involved in review, revision, supervision and funding acquisition.

Data availability

The data supporting this article have been included as part of the ESI.†

Conflicts of interest

The authors declare no conflict of interests.

Acknowledgements

The authors acknowledge the DOD HBCU/MSI instrumentation award (contract #: W911NF1910522) to acquire HR-TEM (JEOL 2100PLUS) with STEM/EDS capability. This work was performed at the Joint School of Nanoscience and Nanoengineering, a member of the Southeastern Nanotechnology Infrastructure Corridor (SENIC) and National Nanotechnology Coordinated Infrastructure (NNCI), supported by the NSF (grant ECCS-1542174). The authors would like to acknowledge funding support from the National Science Foundation for funding of the AccelNet INFRAMES project, as well as the TUCASI Foundation. We are grateful for financial support from the DEVCOM Soldier Center and the UNC ROI program, and the NC Collaboratory.

Notes and references

1 A. F. S. Costa, F. C. G. Almeida, G. M. Vinhas and L. A. Sarubbo, Production of Bacterial Cellulose by Gluconacetobacter Hansenii Using Corn Steep Liquor As Nutrient Sources, *Front. Microbiol.*, 2017, **8**, 2027, DOI: **10.3389/fmicb.2017.02027**.

2 Rahmayetty, M. Yulvianti, M. Toha and N. Kanani, *The Effect of Acetobacter Xylinum Concentration to Bacterial Cellulose Production Using Waste Water of Palm Flour Industry as Fermentation Medium*. In *Proceedings of the 2nd International Conference for Smart Agriculture, Food, and Environment (ICSAFE 2021)*, ed. Huda, N., Jaswir, I., Romdhonah, Y., Alimuddin, A., Ahamed, T. and Nasser, N., Atlantis Press International BV, Dordrecht, 2023, pp. 99–106, DOI: **10.2991/978-94-6463-090-9_12**.

3 E. Meng, C.-L. Chen, C.-C. Liu, C.-C. Liu, S.-J. Chang, J.-H. Cherng, H.-H. Wang and S.-T. Wu, Bioapplications of Bacterial Cellulose Polymers Conjugated with Resveratrol for Epithelial Defect Regeneration, *Polymers*, 2019, **11**(6), 1048, DOI: **10.3390/polym11061048**.

4 R. T. A. Machado, A. B. Meneguin, R. M. Sábio, D. F. Franco, S. G. Antonio, J. Gutierrez, A. Tercjak, A. A. Berretta, S. J. L. Ribeiro, S. C. Lazarini, W. R. Lustri and H. S. Barud, Komagataeibacter Rhaeticus Grown in Sugarcane Molasses-Supplemented Culture Medium as a Strategy for Enhancing Bacterial Cellulose Production, *Ind. Crops Prod.*, 2018, **122**, 637–646, DOI: **10.1016/j.indcrop.2018.06.048**.

5 S. Swingler, A. Gupta, H. Gibson, M. Kowalczuk, W. Heaselgrave and I. Radecka, Recent Advances and Applications of Bacterial Cellulose in Biomedicine, *Polymers*, 2021, **13**(3), 412, DOI: **10.3390/polym13030412**.

6 K. Qiu and A. N. Netravali, A Review of Fabrication and Applications of Bacterial Cellulose Based Nanocomposites, *Polym. Rev.*, 2014, **54**(4), 598–626, DOI: **10.1080/15583724.2014.896018**.

7 S. Baker, S. V. Prudnikova, A. A. Shumilova, O. V. Perianova, S. M. Zharkov and A. Kuzmin, Bio-Functionalization of Phytogenic Ag and ZnO Nanobactericides onto Cellulose Films for Bactericidal Activity against Multiple Drug Resistant Pathogens, *J. Microbiol. Methods*, 2019, **159**, 42–50, DOI: **10.1016/j.mimet.2019.02.009**.

8 M. T. Shaaban, M. Zayed and H. S. Salama, Antibacterial Potential of Bacterial Cellulose Impregnated with Green Synthesized Silver Nanoparticle Against S. Aureus and P. Aeruginosa, *Curr. Microbiol.*, 2023, **80**(2), 75, DOI: **10.1007/s00284-023-03182-7**.

9 W. R. Warren and D. R. LaJeunesse, Characterization of Hydrothermal Deposition of Copper Oxide Nanoleaves on Never-Dried Bacterial Cellulose, *Polymers*, 2019, **11**(11), 1762, DOI: **10.3390/polym11111762**.

10 N. Melnikova, A. Knyazev, V. Nikolskiy, P. Peretyagin, K. Belyaeva, N. Nazarova, E. Liyaskina, D. Malygina and V. Revin, Wound Healing Composite Materials of Bacterial Cellulose and Zinc Oxide Nanoparticles with Immobilized Betulin Diphosphate, *Nanomaterials*, 2021, **11**(3), 713, DOI: **10.3390/nano11030713**.

11 Z. Qin, W. Liu, H. Chen, J. Chen, H. Wang and Z. Song, Preparing Photocatalytic Paper with Improved Catalytic Activity by in Situ Loading Poly-Dopamine on Cellulose Fibre, *Bull. Mater. Sci.*, 2019, **42**(2), 54, DOI: **10.1007/s12034-019-1736-1**.

12 Y. Bi, X. Luo, Y. Yin, F. Tang, H. Sun, L. Huang, L. Chen and J. Li, Robust, Stable Cooling Cellulose Composite: Coupling Nano-SiO2 and Cellulose Acetate in Natural Cellulose, *Int. J. Biol. Macromol.*, 2024, **277**, 133728, DOI: **10.1016/j.ijbiomac.2024.133728**.

13 M. Du, M. Peng, B. Mai, F. Hu, X. Zhang, Y. Chen and C. Wang, A Multifunctional Hybrid Inorganic-Organic Coating Fabricated on Magnesium Alloy Surface with Antiplatelet Adhesion and Antibacterial Activities, *Surf. Coat. Technol.*, 2020, **384**, 125336, DOI: **10.1016/j.surfcoat.2020.125336**.

14 M. Topuz, Y. Akinay, E. Karatas and T. Cetin, $Ti_3C_2T_x$ MXene-Functionalized Hydroxyapatite/Halloysite Nanotube Filled Poly– (Lactic Acid) Coatings on Magnesium: In Vitro and Antibacterial Applications, *J. Magnes. Alloys*, 2024, **12**(9), 3758–3771, DOI: **10.1016/j.jma.2024.09.017**.

15 S. A. Khan, Z. Mohd Zain, Z. Siddiqui, W. Khan, A. Aabid, M. Baig and M. Abdul Malik, Development of Magnesium Aluminate ($MgAl_2O_4$) Nanoparticles for Refractory Crucible Application, *PLoS One*, 2024, **19**(1), e0296793, DOI: **10.1371/journal.pone.0296793**.

© 2025 The Author(s). Published by the Royal Society of Chemistry

Open Access Article. Published on 28 March 2025. Downloaded on 5/19/2026 12:03:56 AM. This article is licensed under a Creative Commons Attribution 3.0 Unported Licence.

16 A. Khalid, H. Ullah, M. Ul-Islam, R. Khan, S. Khan, F. Ahmad, T. Khan and F. Wahid, Bacterial Cellulose–TiO_2 Nanocomposites Promote Healing and Tissue Regeneration in Burn Mice Model, *RSC Adv.*, 2017, **7**(75), 47662–47668, DOI: **10.1039/C7RA06699F**.

17 S. Wu, C. Li, S. Y. Lien and P. Gao, Temperature Matters: Enhancing Performance and Stability of Perovskite Solar Cells through Advanced Annealing Methods, *Chemistry*, 2024, **6**(1), 207–236, DOI: **10.3390/chemistry6010010**.

18 A. Celebioglu, S. Vempati, C. Ozgit-Akgun, N. Biyikli and T. Uyar, Water-Soluble Non-Polymeric Electrospun Cyclodextrin Nanofiber Template for the Synthesis of Metal Oxide Tubes by Atomic Layer Deposition, *RSC Adv.*, 2014, **4**(106), 61698–61705, DOI: **10.1039/C4RA12073F**.

19 J. Škamat, A. Lebedev, O. Černašėjus and R. Stonys, Effect of Thermochemical Boronizing of Alumina Surface on the Borate Crystals Growth and Interaction with Nickel and Nickel Alloy, *Crystals*, 2022, **13**(1), 4, DOI: **10.3390/cryst13010004**.

20 A. Barrera, F. Tzompantzi, J. Campa-Molina, J. E. Casillas, R. Pérez-Hernández, S. Ulloa-Godinez, C. Velásquez and J. Arenas-Alatorre, Photocatalytic Activity of Ag/Al_2 O_3 –Gd_2 O_3 Photocatalysts Prepared by the Sol–Gel Method in the Degradation of 4-Chlorophenol, *RSC Adv.*, 2018, **8**(6), 3108–3119, DOI: **10.1039/C7RA12665D**.

21 Y. Wan, C. Samundsett, J. Bullock, M. Hettick, T. Allen, D. Yan, J. Peng, Y. Wu, J. Cui, A. Javey and A. Cuevas, Conductive and Stable Magnesium Oxide Electron-Selective Contacts for Efficient Silicon Solar Cells, *Adv. Energy Mater.*, 2017, **7**(5), 1601863, DOI: **10.1002/aenm.201601863**.

22 Y. Xu, S. Willis, K. Jordan and E. Sismour, Chitosan Nanocomposite Films Incorporating Cellulose Nanocrystals and Grape Pomace Extracts, *Packag. Technol. Sci.*, 2018, **31**(9), 631–638, DOI: **10.1002/pts.2389**.

23 R. Becerril, C. Nerín and F. Silva, Encapsulation Systems for Antimicrobial Food Packaging Components: An Update, *Molecules*, 2020, **25**(5), 1134, DOI: **10.3390/molecules25051134**.

24 M. D. R. Herrera-Rivera, S. P. Torres-Arellanes, C. I. Cortés-Martínez, D. C. Navarro-Ibarra, L. Hernández-Sánchez, F. Solis-Pomar, E. Pérez-Tijerina and R. Román-Doval, Nanotechnology in Food Packaging Materials: Role and Application of Nanoparticles, *RSC Adv.*, 2024, **14**(30), 21832–21858, DOI: **10.1039/D4RA03711A**.

25 S. Hsieh, J. Hsieh, W. Chen and C. Chuang, Electroless Nickel Deposition for Front Side Metallization of Silicon Solar Cells, *Materials*, 2017, **10**(8), 942, DOI: **10.3390/ma10080942**.

26 M. Shahbazi, H. Jäger, R. Ettelaie, J. Chen, P. A. Kashi and A. Mohammadi, Dispersion Strategies of Nanomaterials in Polymeric Inks for Efficient 3D Printing of Soft and Smart 3D Structures: A Systematic Review, *Adv. Colloid Interface Sci.*, 2024, **333**, 103285, DOI: **10.1016/j.cis.2024.103285**.

27 F. Fahma, N. Hori, T. Iwata and A. Takemura, The Morphology and Properties of Poly(Methyl Methacrylate)-cellulose Nanocomposites Prepared by Immersion Precipitation Method, *J. Appl. Polym. Sci.*, 2013, **128**(3), 1563–1568, DOI: **10.1002/app.38312**.

28 M. Nogi, M. Karakawa, N. Komoda, H. Yagyu and T. T. Nge, Transparent Conductive Nanofiber Paper for Foldable Solar Cells, *Sci. Rep.*, 2015, **5**(1), 17254, DOI: **10.1038/srep17254**.

29 F. Guan and C. F. Guo, Flexible, High-Strength, and Porous Nano-Nano Composites Based on Bacterial Cellulose for Wearable Electronics: A Review, *Soft Sci.*, 2022, **2**(3), 16, DOI: **10.20517/ss.2021.19**.

30 V. Girard, J. Chaussé and P. Vermette, Bacterial Cellulose: A Comprehensive Review, *J. Appl. Polym. Sci.*, 2024, **141**(15), e55163, DOI: **10.1002/app.55163**.

31 *Thermal Analysis of Polymers: Fundamentals and Applications*, ed. Menczel, J. D. and Prime, R. B., Wiley, 1st edn, 2009, DOI: **10.1002/9780470423837**.

32 S. Silviana and A. Ni'Matus Sa'Adah, Mechanical and thermal properties of bacterial cellulose reinforced with bamboo microfibrillated cellulose and plasticized with epoxidized waste cooking oil, *Cellul. Chem. Technol.*, 2022, **56**(3–4), 331–339, DOI: **10.35812/CelluloseChemTechnol.2022.56.29**.

33 J. George, K. V. Ramana, S. N. Sabapathy, J. H. Jagannath and A. S. Bawa, Characterization of Chemically Treated Bacterial (Acetobacter Xylinum) Biopolymer: Some Thermo-Mechanical Properties, *Int. J. Biol. Macromol.*, 2005, **37**(4), 189–194, DOI: **10.1016/j.ijbiomac.2005.10.007**.

34 L. C. Thomas *Interpreting Unexpected Events and Transitions in DSC Results (TA039)*. Retrieved from **https://www.tainstruments.com**.

35 S. S. Milani, M. G. Kakroudi, N. P. Vafa, S. Rahro and F. Behboudi, Synthesis and Characterization of $MgAl_2O_4$ Spinel Precursor Sol Prepared by Inorganic Salts, *Ceram. Int.*, 2021, **47**(4), 4813–4819, DOI: **10.1016/j.ceramint.2020.10.051**.

36 S. B. Schröpfer, M. K. Bottene, L. Bianchin, L. C. Robinson, V. D. Lima, V. D. Jahno, H. D. S. Barud and S. J. L. Ribeiro, Biodegradation Evaluation of Bacterial Cellulose, Vegetable Cellulose and Poly (3-Hydroxybutyrate) in Soil, *Polímeros*, 2015, **25**(2), 154–160, DOI: **10.1590/0104-1428.1712**.

37 D. Rahmadiawan, H. Abral, M. A. Azka, S. M. Sapuan, R. I. Admi, S.-C. Shi, R. Zainul, A. Azril, A. Zikri and M. Mahardika, Enhanced Properties of TEMPO-Oxidized Bacterial Cellulose Films via Eco-Friendly Non-Pressurized Hot Water Vapor Treatment for Sustainable and Smart Food Packaging, *RSC Adv.*, 2024, **14**(40), 29624–29635, DOI: **10.1039/D4RA06099G**.

38 K. Lukas and P. K. LeMaire, Differential Scanning Calorimetry: Fundamental Overview, *Resonance*, 2009, **14**(8), 807–817, DOI: **10.1007/s12045-009-0076-7**.

39 H. S. Barud, C. A. Ribeiro, M. S. Crespi, M. A. U. Martines, J. Dexpert-Ghys, R. F. C. Marques, Y. Messaddeq and S. J. L. Ribeiro, Thermal Characterization of Bacterial Cellulose–Phosphate Composite Membranes, *J. Therm. Anal. Calorim.*, 2007, **87**(3), 815–818, DOI: **10.1007/s10973-006-8170-5**.

40 A. Mettler-Toledo *Application of Thermal Analysis to Flavors and Fragrances*, 2013. Retrieved from **https://www.mt.com/dam/LabDiv/guides-glen/ta-ff-wp/ta_applications_ff_EN.pdf**.

41 C. J. Grande, F. G. Torres, C. M. Gomez and M. Carmen Bañó, Nanocomposites of Bacterial Cellulose/Hydroxyapatite for Biomedical Applications, *Acta Biomater.*, 2009, **5**(5), 1605–1615, DOI: **10.1016/j.actbio.2009.01.022**.

© 2025 The Author(s). Published by the Royal Society of Chemistry

Open Access Article. Published on 28 March 2025. Downloaded on 5/19/2026 12:03:56 AM.
This article is licensed under a Creative Commons Attribution 3.0 Unported Licence.

42 N. Folmann Lima, G. M. Maciel, I. De Andrade Arruda Fernandes and C. Windson Isidoro Haminiuk, Optimising the Production Process of Bacterial Nanocellulose: Impact on Growth and Bioactive Compounds, *Food Technol. Biotechnol.*, 2023, **61**(4), 494–504, DOI: **10.17113/ftb.61.04.23.8182**.

43 A. R. Molla, C. R. Kesavulu, R. P. S. Chakradhar, A. Tarafder, S. K. Mohanty, J. L. Rao, B. Karmakar and S. K. Biswas, Microstructure, Mechanical, Thermal, EPR, and Optical Properties of $MgAl_2O_4$:Cr^{3+} Spinel Glass–Ceramic Nanocomposites, *J. Alloys Compd.*, 2014, **583**, 498–509, DOI: **10.1016/j.jallcom.2013.08.122**.

44 Y. Wang, X. Xie and C. Zhu, Self-Propagating High-Temperature Synthesis of Magnesium Aluminate Spinel Using Mg–Al Alloy, *ACS Omega*, 2022, 7(15), 12617–12623, DOI: **10.1021/acsomega.1c06583**.

45 P. B. Raja, K. R. Munusamy, V. Perumal and M. N. M. Ibrahim, Characterization of Nanomaterial Used in Nanobioremediation, In *Nano-Bioremediation: Fundamentals and Applications*, Elsevier, 2022, pp. 57–83, DOI: **10.1016/B978-0-12-823962-9.00037-4**.

46 S. B. Khan, N. Li, S. Chen, J. Liang, C. Xiao and X. Sun, Influence of Nanoparticle Size on the Mechanical and Tribological Characteristics of TiO2 Reinforced Epoxy Composites, *J. Mater. Res. Technol.*, 2023, **26**, 6001–6015, DOI: **10.1016/j.jmrt.2023.09.002**.

47 Y. Sahu and S. Agrawal, Structural Features, Dielectric Behaviour of Spinel Type Magnesium Aluminate Synthesized by the Auto-Combustion Method, *J. Phys. Conf. Ser.*, 2023, **2576**(1), 012006, DOI: **10.1088/1742-6596/2576/1/012006**.

48 Y. N. Nguyen, A.-T. Dao, M.-H. Le, K. Q. Dang and M. Nanko, Fabrication of transparent $MgAl_2O_4$ spinel ceramics by pecs processing of combustion - sythesized nanopowders, *Acta Metall. Slovaca*, 2019, **25**(3), 186–192, DOI: **10.12776/ams.v25i3.1313**.

49 K. Potivara and M. Phisalaphong, Development and Characterization of Bacterial Cellulose Reinforced with Natural Rubber, *Materials*, 2019, **12**(14), 2323, DOI: **10.3390/ma12142323**.

50 M. Poletto, V. Pistor and A. J. Zattera, Structural Characteristics and Thermal Properties of Native Cellulose, in *Cellulose - Fundamental Aspects*, ed. Van De Ven, T. G. M., InTech, 2013, DOI: **10.5772/50452**.

51 H. Ullah, F. Wahid, H. A. Santos and T. Khan, Advances in Biomedical and Pharmaceutical Applications of Functional Bacterial Cellulose-Based Nanocomposites, *Carbohydr. Polym.*, 2016, **150**, 330–352, DOI: **10.1016/j.carbpol.2016.05.029**.

52 O. Shezad, S. Khan, T. Khan and J. K. Park, Physicochemical and Mechanical Characterization of Bacterial Cellulose Produced with an Excellent Productivity in Static Conditions Using a Simple Fed-Batch Cultivation Strategy, *Carbohydr. Polym.*, 2010, **82**(1), 173–180, DOI: **10.1016/j.carbpol.2010.04.052**.

53 J. Fang, S. Kawano, K. Tajima and T. Kondo, In Vivo Curdlan/Cellulose Bionanocomposite Synthesis by Genetically Modified Gluconacetobacter Xylinus, *Biomacromolecules*, 2015, **16**(10), 3154–3160, DOI: **10.1021/acs.biomac.5b01075**.

54 M. Choi, Y.-R. Kang, I.-S. Lim and Y. H. Chang, Structural Characterization of Cellulose Obtained from Extraction Wastes of Graviola (Annona Muricata) Leaf, *Prev. Nutr. Food Sci.*, 2018, **23**(2), 166–170, DOI: **10.3746/pnf.2018.23.2.166**.

55 M. Ul-Islam, W. A. Khattak, M. W. Ullah, S. Khan and J. K. Park, Synthesis of Regenerated Bacterial Cellulose-Zinc Oxide Nanocomposite Films for Biomedical Applications, *Cellulose*, 2014, **21**(1), 433–447, DOI: **10.1007/s10570-013-0109-y**.

56 J. Sugiyama, J. Persson and H. Chanzy, Combined Infrared and Electron Diffraction Study of the Polymorphism of Native Celluloses, *Macromolecules*, 1991, **24**(9), 2461–2466, DOI: **10.1021/ma00009a050**.

57 A. M. Gallardo-Moreno, M. L. Navarro-Pérez, V. Vadillo-Rodríguez, J. M. Bruque and M. L. González-Martín, Insights into Bacterial Contact Angles: Difficulties in Defining Hydrophobicity and Surface Gibbs Energy, *Colloids Surf., B*, 2011, **88**(1), 373–380, DOI: **10.1016/j.colsurfb.2011.07.016**.

58 I. Indriyati, N. Frecilla, B. W. Nuryadin, Y. Irmawati and Y. Srikandace, Enhanced Hydrophobicity and Elasticity of Bacterial Cellulose Films by Addition of Beeswax, *Macromol. Symp.*, 2020, **391**(1), 1900174, DOI: **10.1002/masy.201900174**.

59 E. Morales-Narváez, H. Golmohammadi, T. Naghdi, H. Yousefi, U. Kostiv, D. Horák, N. Pourreza and A. Merkoçi, Nanopaper as an Optical Sensing Platform, *ACS Nano*, 2015, **9**(7), 7296–7305, DOI: **10.1021/acsnano.5b03097**.

60 B. Dursun, T. Sar, A. Ata, M. Morcrette, M. Y. Akbas and R. Demir-Cakan, Pyrolyzed Bacterial Cellulose-Supported SnO2 Nanocomposites as High-Capacity Anode Materials for Sodium-Ion Batteries, *Cellulose*, 2016, **23**(4), 2597–2607, DOI: **10.1007/s10570-016-0966-2**.

61 M. Raut, E. Asare, S. Syed Mohamed, E. Amadi and I. Roy, Bacterial Cellulose-Based Blends and Composites: Versatile Biomaterials for Tissue Engineering Applications, *Int. J. Mol. Sci.*, 2023, **24**(2), 986, DOI: **10.3390/ijms24020986**.

62 Q. Li, Y. Zhang, Z. Liu, S. Liu, F. Huang and M. Zheng, Novel Bacterial Cellulose-TiO2 Stabilized Pickering Emulsion for Photocatalytic Degradation, *Cellulose*, 2022, **29**(9), 5223–5234, DOI: **10.1007/s10570-022-04604-8**.

63 R. Brandes, E. C. A. Trindade, D. F. Vanin, V. M. M. Vargas, C. A. Carminatti, H. A. Al-Qureshi and D. O. S. Recouvreux, Spherical Bacterial Cellulose/TiO2 Nanocomposite with Potential Application in Contaminants Removal from Wastewater by Photocatalysis, *Fibers Polym.*, 2018, **19**(9), 1861–1868, DOI: **10.1007/s12221-018-7798-7**.

64 N. Melnikova, A. Knyazev, V. Nikolskiy, P. Peretyagin, K. Belyaeva, N. Nazarova, E. Liyaskina, D. Malygina and V. Revin, Wound Healing Composite Materials of Bacterial Cellulose and Zinc Oxide Nanoparticles with Immobilized Betulin Diphosphate, *Nanomaterials*, 2021, **11**(3), 713, DOI: **10.3390/nano11030713**.

© 2025 The Author(s). Published by the Royal Society of Chemistry